Improving the photocatalytic performance of cobalt-doped titania nanosheets by induced oxygen vacancies for efficient degradation of organic pollutants

Islam G. Alhindawy [a], Emad A. Elshehy [a,*], Ahmed O. Youssef [b], S. M. Abdelwahab [b], Ahmed A. Zaher [c], Waleed A. El-Said [d,e], Hamed I. Mira [a], and Amr M. Abdelkader [f,*]

[a] *Nuclear Materials Authority, El Maadi, Cairo, Egypt*
[b]*Department of Chemistry, Faculty of Science, Ain Shams University, Cairo, Egypt*
[c]*Department of Chemistry, Faculty of Science, Mansoura University, Elmansoura, Egypt*
[d]*Department of Chemistry, Faculty of Science, Assiut University, Assiut, 71516, Egypt*
[e]*University of Jeddah, College of Science, Department of Chemistry, PO Box 80327, Jeddah 21589, Saudi Arabia*
[f]*Department of Engineering, Bournemouth University, Talbot Campus, Fern Barrow, Poole, BH12 5BB, United Kingdom.*
**Corresponding authors: Amr Abdelkader (aa494@cam.ac.uk)*

ABSTRACT:

Photocatalytic degradation using Co_3O_4-TiO_2-based catalysts has shown promising results in removing organic and inorganic pollutants under UV light. Introducing defects is believed to increase the charge carrier mobility and the coordinatively active sites that are usually also catalytically active sites, leading to improving the catalytic performance. This work carefully designed a nanostructure based on interconnected cobalt-doped titanium dioxide thin nanosheets. We engineered defects in the oxygen sits by partial carbothermal reduction that enhanced the photocatalytic performance of the prepared nanostructure. The degradation of methyl orange as a model for organic pollutants was studied. The results proved that the designed photocatalyst could remove methyl orange fully under UV light within a few minutes and an initial concentration of up to 200 mg/l.

Keywords: Nanomaterials; composites; titanium oxide; photocatalytic degradation; two-dimensional materials; Methyl orange.

1. Introduction

Semiconductor photocatalytic processes have gained a great deal of interest for removing a wide range of water pollutants due to their low cost, simplicity, and environmental compatibility. Photocatalysis uses sunlight to decompose organic and inorganic pollutants [1]**.** Semiconductor photocatalysis generates electron-hole pairs that can oxidise or reduce pollutants in the solution and remove them from the system when absorbing photons. Up to now, enormous types of semiconductors photocatalyst have been widely developed, including; metal oxides (TiO_2, Cu_2O, ZnO, Fe_2O_3, and Ag_2O), metal sulphides (CDs, MoS_2, and ZnS), multicomponent oxides (Bi_2WO_6, $KTiNbO_5$, $K_4Nb_6O_{17}$, $BiVO_4$, and $SrTiO_3$), and graphitic carbon nitride (g-C_3N_4) [2-9]. Nanostructures based on titanium oxide were widely used as a photocatalyst to degrade several organic compounds since they are inexpensive, easy to process, and easy to tune the inherent ability to photoactivate reactions without affecting the chemical and thermal stability [8-10]. Pure TiO_2 exists in three different polymorphs with different bandgap energies; rutile (3.0 eV), anatase (3.2 eV), and brookite (~3.2 eV) [11]. Many have published work to tune the TiO_2 bandgap by, for example, doping with other ions or inducing other types of defects. These strategies helped activate TiO_2 at the visible light region, unlike pristine TiO_2, which is active in the UV region and uses only <5% of the solar light. Doping with transition metal oxides and noble metals compounds has been pursued and successfully generates visible light TiO_2 photocatalysis [10-18].

Amongst these dopants, cobalt oxides are receiving particular interest based on their success in the photo-reduction of CO_2 in visible light and dye-sensitised solar cells for power generation. Although Co-doped TiO_2 and Co-Ti binary oxides were reported to enhance the electrocatalytic performance in the visible light region, several challenges still need to be addressed to obtain the full potential of the Co/TiO_2 system. First, some have reported fast carrier recombination, resulting in low photocatalytic activities. Second, the multi-valence nature of cobalt oxides renders the produced photocatalysis sub-stable to a number of oxidation/reduction processes, which reduces the stability and catalytic efficiency over the long run. Third, the hydrophilic of TiO_2, with a water contact angle approaching 0°, was reported to be reduced by cobalt doping.

Reducing the hydrophilicity means higher energy requires to overcome the barriers at the solid/liquid interface, slowing the kinetic of the overall photocatalytic reactions. Finally, another problem is recovering the photocatalysis, particularly nanoparticles, after the end of the process [19-21].

The concept we are introducing in this paper is based on the careful design of a 3D porous nanostructure of Co-Ti oxides interconnected nanoparticles by a carbon layer ($Co/TiO_2@C$). In this system, the inherent photocatalytic activity of the Co-Ti oxides is enhanced by two mechanisms; (a) oxygen vacancies induced by controlled carbothermal deoxidation during materials synthesis and (b) the conductive carbon layers that promote charge transfer and separation. The synthesis method, consisting of hydrothermal and heat treatment steps, allows the in-situ partial reduction by the carbon generated from glucose. By taking water contaminated by MO dye as a proof-of-concept, $Co/TiO_2@C$ was able to remove most of it from the solution in a few minutes. The removal mechanism was also studied and believed to be by the oxidative degradation of MO by $Co/TiO_2@C$.

2-Experimental:

2.1 Chemicals

Titanium isopropoxide $Ti[OCH(CH_3)_2]_4$**,** cobalt acetate $(CH_3CO_2)_2Co$**,** potassium chloride (KCl)**,** ethanol, glucose, and methyl orange dye were purchased from Sigma-Aldrich.

2.2 Catalysts preparation

2.2.1 Synthesis of TiO_2 nanoparticles

A 100 ml ethanol was mixed with 0.5 mL of 0.1 M of aqueous KCl, followed by adding 1.5 ml of titanium isopropoxide under stirring for 4 h. Then the solution was transferred into a 100-ml Teflon-lined stainless autoclave and heated at 170 °C for 30 h. The autoclave was then air-cooled to room temperature. The resulting product was collected and washed thoroughly with ethanol and dried at 60 °C in an oven. Finally, the precipitate was calcined at 500 °C for 3 h to obtain TiO_2 nanoparticles.

2.2.2 Synthesis of Co-doped TiO_2 (Co/TiO_2) nanocomposite

A 100 mL ethanol was mixed with 0.5 mL of aqueous KCl (0.1 M), followed by adding a 0.88 gm of cobalt acetate, then 1.5 ml of titanium isopropoxide was added under stirring for 4 h. The solution was then moved into a 100-mL Teflon-lined stainless autoclave, heated at 170 °C for 30 h and air-cooled to room temperature. The resulting product was collected and washed thoroughly with ethanol and dried at 60 °C in an oven. Finally, the product was calcined at 500 °C for 3h to obtain Co/TiO_2 nanocomposites.

2.2.3 Synthesis of Co-doped TiO_2 @C nanocomposite

A 0.42 gm of the synthesised Co/TiO_2 nanocomposites was dispersed in 75 ml H_2O that contained 0.0189 gm of glucose. The mixture was mixed under stirring for 2 h, then transferred into a 100-ml Teflon-lined stainless autoclave. The autoclave was maintained at 170 °C for 20 h and then air-cooled to room temperature. The resulting product was collected and washed thoroughly with water and finally dried at 60 °C in an oven, then calcined the product at 500 °C for 3h to obtain Co/TiO_2@C nanocomposites.

2.3 Degradation process

A wooden box of lengths of 40 x 55 x 60 (cm) was used for achieving the degradation process was completely sealed and painted on the inside with black colour, and inside it was installed on the top a 43 cm UV lamp with a wavelength of 350 nm. A magnetic stirrer was placed inside it to be used in the stirring process (Fig. S1). The degradation experiments were carried out using the batch method to evaluate the degradation activities of the synthesised materials toward methyl orange from aqueous solutions under UV light. Ten milligrams of each of the aforementioned materials were added to 10 mL solutions with 100 mg L^{-1} MO. After shaking under UV light for an appropriate time at home temperature, the catalysts were collected by filtration. The concentrations of the MO aqueous solution were determined before and after degradation using a spectrophotometer.

3- Results and Discussion

3.1 Materials Characterization

XRD diffraction was used to investigate the phase compositions of the prepared samples (Fig. 1a). The XRD pattern of TiO_2 shows all the characteristic peaks for anatase (JCPDS 21-1272) [22]. Figure 1(a) showed the XRD patterns of Co/TiO_2 and Co/TiO_2@C nanocomposites, which indicates no free cobalt phases, suggesting all the cobalt is dissolved in the anatase crystallites. The lack of any obvious carbon peaks can be referred to as the low crystallinity of carbon in the composite. Interestingly, the diffraction patterns of Co/TiO_2 and Co/TiO_2@C samples are similar to that of pure TiO_2, with a slight shifting in the peak positions. This shift is due to changes in the local structure around Ti^{4+} after Co^{3+} and Co^{2+} substitution, further suggesting the Co dissolution in the lattice. Another deviance of the Co incorporation can be obtained from the TiO_2 colour change with cobalt content. The broad peaks in all the XRD patterns suggested the nanosized particles of pure TiO_2 did not change after adding Co or carbon. The crystal size of pure TiO_2, Co/TiO_2, nanocomposite and Co/TiO_2@C nanocomposite samples was 9.87, 11.30, and 11.38 nm, respectively, as calculated by Scherrer's equation. The increase in crystal size of the Co-Ti samples further confirms that cobalt is replacing Ti in the anatase lattice. From the (101) XRD peaks as magnified in Fig. 1b, one can see that the peaks substantially shift to higher 2 theta with the doping of Co and C, and the crystallite size of C-Co-doped TiO_2 is larger compared with Co-doped TiO_2 material. These results indicate that carbon and cobalt have a synergistic effect on each other. Compared with cobalt doped TiO_2, the crystallite size and the position of diffraction peaks of Co-doped TiO_2 show little differences, implying that the impact of carbon doping on the crystal structure is slight.

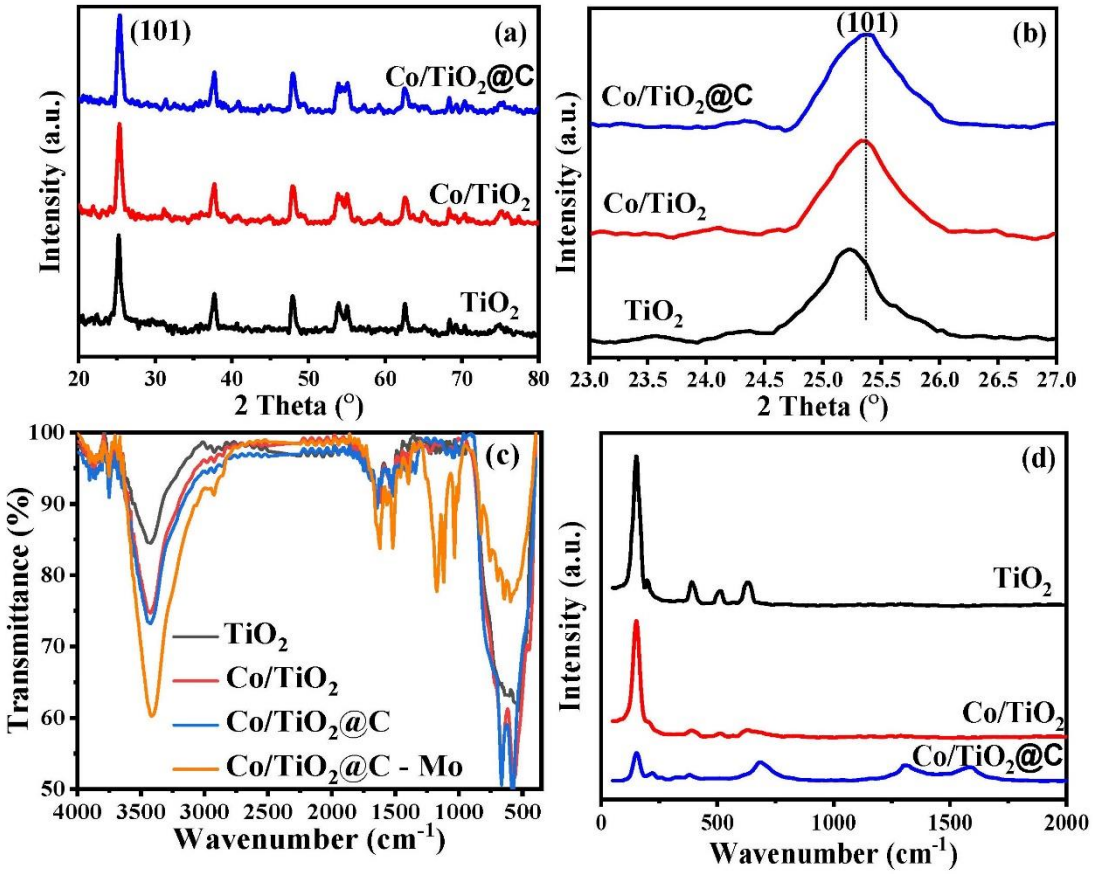

Fig. 1 (a) XRD diffraction pattern (b) FTIR spectra for TiO_2 NPs, Co/TiO_2 nanocomposite, Co/TiO_2@C nanocomposite, Co/TiO_2@C catalytic after MO dye degradation. (c) Raman spectra of TiO_2 NPs, Co/TiO_2 nanocomposite and Co/TiO_2@C nanocomposite.

The chemical composition and the surface functional groups of the photocatalysts were determined by FT-IR and Raman analysis. Figure 1(c&d)) shows the obtained FTIR spectra of the synthesised materials. All the FTIR spectra showed a vibration band at 3425cm^{-1} that could be attributed to the stretching vibration of the O-H group. This peak intensity increases with the cobalt doping and the treatment with carbon, implying an improvement in the interaction between water and the photocatalysts. The vibration peak at 1643 cm^{-1} can be assigned for the adsorbed water molecules onto the surface of the nanoparticles. The vibration band at around 1396 cm^{-1} belongs to the C-H bond [23]. The low-frequency broadband located in the range 400–800 cm^{-1} corresponds to the Ti-O-Ti vibrational mode. Interestingly, an increase of this band intensity for both Co and C doped TiO_2 indicates structure defects. The band shift can also be attributed to Co-O bonds, following Ti^{4+} substitution with Co^{2+} and Co^{3+} within the TiO_2

lattice. Therefore, the bonding system found inside the pure anatase TiO_2 NPs was affected by doping with Co or/and carbon (Fig. 1b).

Figure 1(d) displays the Raman spectra of the TiO_2, Co/TiO_2 and Co/TiO_2@C recorded in the range 50–3000 cm^{-1}. The peaks at 151, 390, 510 and 627cm^{-1} could be assigned to Eg, B1g, A1g, and Eg modes of anatase phase, respectively [19]. After doping with Co, the intensity of the B1g, A1g, and Eg peaks significantly decreased with some shift. Although these results suggest that the Co did not completely change the anatase phase, it also implies significant distortion in the long-order crystallite, consistent with the XRD results. This distortion could be attributed to the substitution of Ti^{4+} by Co^{3+} and the difference between their ionic charges. Also, Co-doping is associated with generating oxygen vacancies, which strongly influences the Ti–O vibration. It should be noted here that the peak position shift is limited because of the nanoscale crystallite size (~25nm), which affects the frequency of shifting due to the phonon confinement. After sintering with the carbon source, a new peak at ~ 232 appeared in the spectrum taken for the composite may be attributed to either disorder-induced scattering or a second-order effect. There is also a clear shift in the A1g peak position and a significant increase in its intensity. Since the A1g peak was previously linked to the oxygen defects in anatase, the changes in its position and intensity suggest creating more oxygen vacancies, probably by the reaction with carbon. The high Raman signal at 689 cm^{-1} suggests that the Eg modes of anatase have been phase shifted because of carbon and cobalt doping [24]. Detecting peaks at the positions of D and G bands (at ~1300 cm^{-1}, 1850 cm^{-1}, respectively) confirms the presence of carbon despite the calcination with Ti-Co oxides in the air. The peaks intensity ratio I_D/I_G is 1.33, suggesting the carbon is likely in an amorphous phase [25].

SEM images of pure TiO_2 NPs and TiO_2 doped with cobalt nanocomposite after calcination at 500 °C are presented in Figs. S2(a) and S3(a). The SEM images with different magnifications of Co/TiO_2@C nanocomposite after calcination at 500 °C are also presented in Fig 2. The results confirm the formation of nanoparticles clusters in all samples. Interestingly, Co-Ti oxide and Co/TiO_2 @C nanoparticles cluster to form 2D sheets. In comparison, Fig. S2 shows that undoped TiO_2 nanoparticles tend to cluster in more irregular shapes. The obvious nanosheets

after the Co and carbon addition suggest preferential growth directions. This is very likely due to the increase in the density of state in the direction perpendicular to C-axes after Co doping and partial oxygen removal by carbon. The 2D sheets are lightly linked together, forming a porous Zig-Zag structure, as can be seen from Fig. 2(a). More details on the morphology of the prepared materials can be gathered from the TEM images (Figs. S2(b), S3(b), and 2(c)). The results showed that all the three tested materials are composed of nanoparticles with parallel facets and an average size of approximately 25 nm. With the addition of Co, the particles start to sinter together at the edges forming 2D nanosheets. The size of the nanoparticles clusters increased with the addition of the carbon sources, without obvious growth of the nanoparticles' size or distortion of their morphology. The presence of cobalt and carbon elements is observed in the EDX spectra of the single-doped and Co-doped materials. The XRD patterns did not show any peaks related to Co and C. Therefore, it may be concluded that Co and carbon ions are uniformly dispersed among the anatase crystallites. The elemental composition can be determined for TiO_2 to be 61.9% (Ti) and 38.1% (O) (Fig. S2 (c-f)). While for Co/TiO_2 composite can be determined to be 56.1% (Ti), 40.2% (O) and 3.7 % (Co) (Fig. S3(c-f). While for Co/TiO_2@C composite to be 55.4% (Ti), 3.6% (Co), 36.1% (O) and 4.7 % (C) (Fig. 2d).

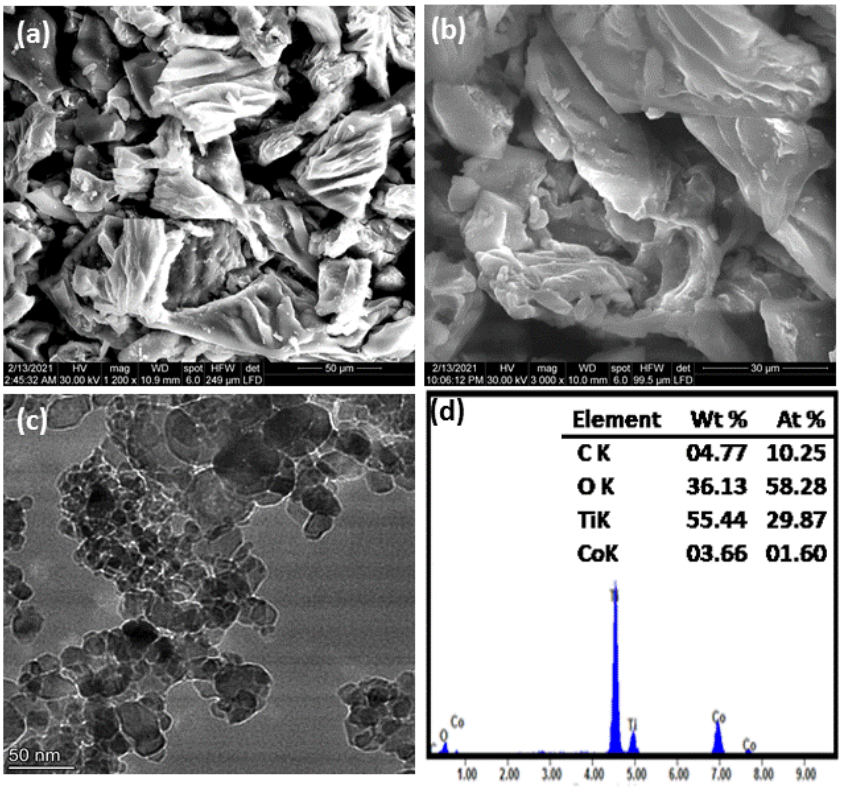

Fig. 2 (a&b) Scanning Electron Microscope (SEM) images with different magnifications, (c) Transmission electron microscope micrograph (TEM), and (d) energy dispersive X-ray (EDX) of the synthesised Co/TiO_2@C nanocomposite.

The N_2 adsorption−desorption isotherms of TiO_2 NPs, cobalt doped TiO_2 nanocomposite and Co/TiO_2@C nanocomposite at 77 K are given in Fig. 3(a). All samples isotherms are typical for type IV isotherms according to the IUPAC classification. The isotherms exhibit hysteresis at a relative pressure above 0.7, implying the presence of a large number of mesopores [26]. The isotherm also shows an abrupt rise at low pressure that corresponds to the adsorption at micropores. Thus, it can be concluded that there is a multilayer range of physisorption isotherms as a result of hierarchal porous structure with nanochannels between the oxides particles. The calculated specific surface areas of TiO_2, Co/TiO_2 and Co-TiO_2@C are 54.861 m^2g^{-1}, 58.006 m^2g^{-1} and 60.946 m^2g^{-1}, respectively. These findings suggest some new pores are introduced to the structure due to the Co-doping and calcination with carbon. One explanation for the increase in the specific surface area could be due to the oxygen or COx gases leaving the oxide structures, which is associated with the formation of oxygen vacancies. Also, the arrangement of the nanoparticles into 2D nanosheets minimises their aggregation and open more surfaces.

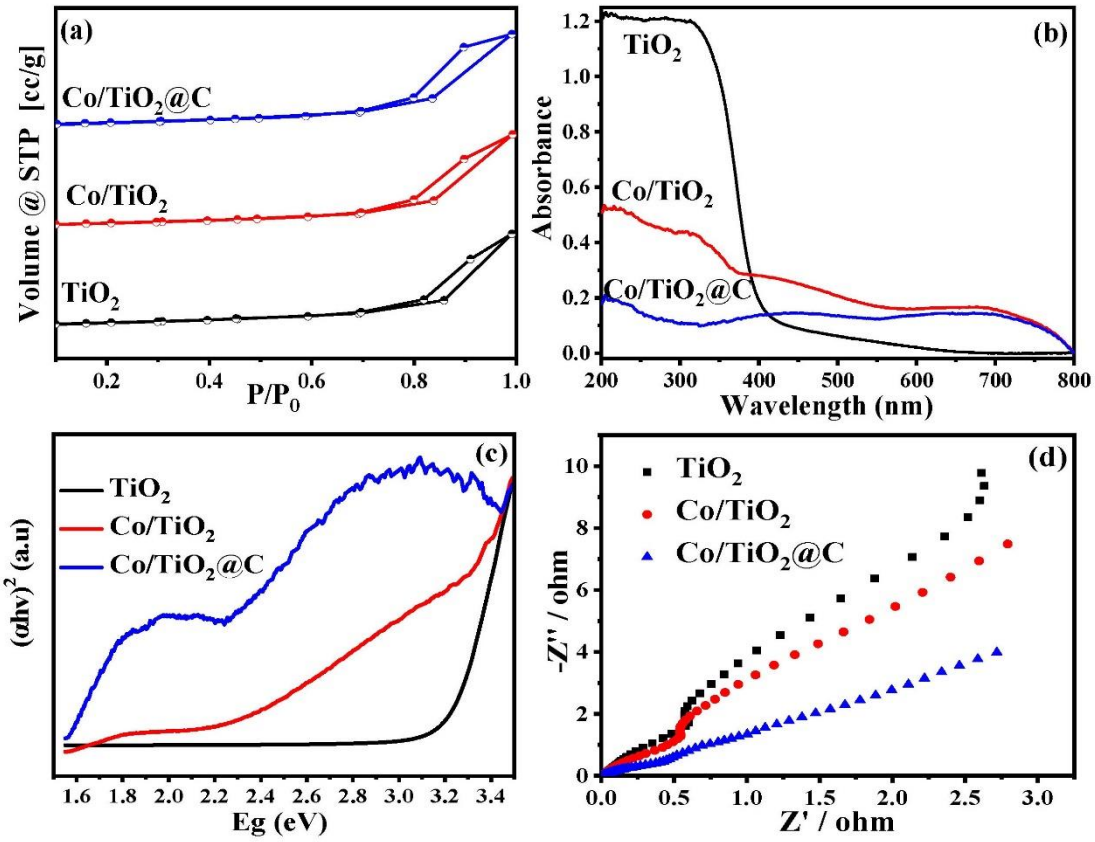

211

212 **Fig. 3** (a) BET isotherms of TiO_2, Co/TiO_2 and Co/TiO_2@C, (b) UV–Visible spectroscopy,
213 (c) is the energy bandgap of TiO_2, Co-doped TiO_2, Co/TiO_2 @C, (e) EIS plots of of TiO_2,
214 Co/TiO_2 and Co/TiO_2@C.

215 UV–Vis spectroscopy can be used to understand the substitution effect of dopant on host
216 lattice and its coordination chemistry. The UV-Vis spectra of pure TiO_2 and Co-doped TiO_2 are
217 shown in (Fig. 3b). Anatase has an absorption peak that occurs at 363 nm corresponds to the
218 intrinsic band–band transition. After doping with Co, the adsorption peak shifted to 495, and
219 one extra peak appeared in the visible region at 582 nm. The peak at lower wavelength was
220 previously attributed to the $^6A_{1g}(S)$ to $^4A_{1g}(G)$, $^4E_g(G)$, and $A_{1g}(S)$ to $^4T_{2g}(G)$ transition, while
221 the peak at 582 nm is for the $^6A_{1g}(S)$ to $^4T_{1g}(G)$ transition of Co^{2+} in octahedral coordination
222 [27]. In the case of TiO_2, each Ti^{4+} is coordinated with six oxygen atoms. When $^{Co2+}$ substitute^{s}
223 $^{Ti4+}$, the electrons in the d-orbital of Co^{2+} will undergo repulsion, which results in the splitting
224 of d-orbitals of Co^{2+}, further confirming Co^{2+} is inside the lattice. To determine the energy
225 bandgap, the linear portion of the Tauc's plot is fitted and extrapolated for zero absorbance, i.e.,
226 F[R] = 0. The energy bandgap of the prepared pure TiO_2 is 3.2 eV, which decreased to 1.93 eV

after doping with Co. After sintering the sample with carbon, the bandgap reduced significantly to 1.6 eV, which could be ascribed to the defect structure (oxygen vacancies) in the titania that introduces additional energy levels in the forbidden zone (Fig. 3c). The origin of such energy levels might be the change in the local distribution around Ti^{4+} or partial conversion of Ti^{4+} to Ti^{3+} and the creation of oxygen vacant sites. Several other groups also observed the bandgap narrowing after doping TiO_2 with Coch groups. However, the bandgap narrowing is more pronounced in the current work correctly because of the lower particles size and the synergy between the Co substitution and the oxygen vacancies induced by the controlled carbothermal reaction.

Electrochemical impedance spectroscopy (EIS) was implemented to reflect the interfacial transfer efficiency of the TiO_2, Co/TiO_2 and Co/TiO_2@C samples. As Fig. 3d shows, the Co/TiO_2@c composite has a smaller radius in the Nyquist plots than oxides without carbon source addition. These results indicate that the induced oxygen vacancies after the carbothermal reduction enhance the separation efficiency of the photogenerated charges and facilitate the interfacial charge transfer [28-31]. As shown in Fig. S4, XPS was performed on Co/TiO_2@C at room temperature to further assess the likelihood of Ti and Co's secondary phases, oxygen deficit, and oxidation states in the near-surface area. The survey peaks (Fig. S4a) are assigned to Ti2p, Co2p, O1s, and C1s elements. Figures S4b, and S4c show the oxidation states of Ti2p and Co2p, which showed the existence of titanium in Ti^{+4}, Ti^{+3}, and Ti^{+2}, as well as cobalt in Co^{+3} and Co^{+2}. Figure S4d, and S4e also display O1s and C1s, confirming induce oxygen vacancies.

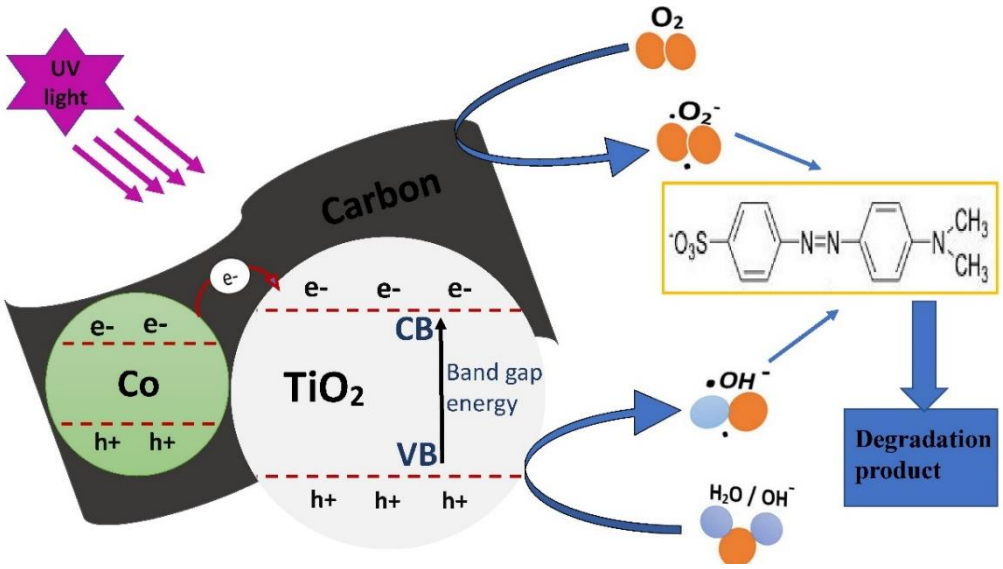

Fig. 4 Possible mechanism of photocatalytic degradation of MO by Co/TiO_2@C.

3.2 Photocatalytic activity of synthesised catalysts

We then investigated the role of cobalt doping and the induced vacancies in improving the photocatalytic activities of TiO_2. The photocatalytic activity of Co/TiO_2@C was evaluated through the degradation of MO under UV light irradiation. UV–visible spectra were used to monitor the change in MO concentrations at λ_{max} = 482 nm (Fig**.** 4) after the treatment. After adding 10 mg of the photocatalysts, a sharp reduction in the MO concentration/decolourisation can be observed after a few minutes of light irradiation. The decrease in peak intensity at λ_{max} = 482 nm can be attributed to the N=N bond of the MO as a result of the catalytic photodegradation (Fig. 4). Figure 5a shows the peaks intensity decreased in the order: Co/TiO_2@C << Co/TiO_2 < TiO_2. Since lower intensities is associated with higher e^- and h^+ separation efficiency, the results indicate an increase in the photocatalytic activity with Co-doping and the partial carbothermal reduction. The peak position did not show obvious shifts indicating the photodegradation proceeds without the generation of toxic intermediates. It should also note that the controlled experiment where Co/TiO_2@C was added without light irradiation (i.e. dark) showed no significant change in the MO concentration within the timeframe of the experiments (Fig. 5a). Also, the preliminary control experiments conducted in the absence of catalyst showed that less than 1.0 % of MO was degraded after 1 h UV

irradiation, indicating that MO has a good photo-stability under light irradiation. Therefore, it can be concluded that a great portion of MO has been removed by photocatalytic degradation rather than physiochemical adsorption on the surface of the nanostructured hybrid.

The pH is a crucial factor for photocatalytic degradation processes because the pH of the solution influences the catalyst surface charge. To clarify the effect of pH on the degradation rate, we measured zeta potentials of the synthesised photocatalysts at different pH values. Fig. 5(b) shows that the point of zero charge (pzc) of TiO_2, Co/TiO_2, and Co/TiO_2@C are at pH 6.5, 6.7, and 7.1, respectively. The minor shifts in the pzc to higher pH values, relative to the pzc of undoped TiO_2 (pH 6.5), confirm the success of Co doping and the induced defects by the carbothermal treatments. These results agree with the FTIR spectra in Fig. 1(c), as the increase in absorption of the O-H group at 3425 cm^{-1} confirms the pH_{pzc} results. When the pH value of the solutions is less than the pH_{PZC} value of the catalyst, the surface of the synthesised photocatalyst becomes positive, and on the contrary, when the pH value of the solution is greater than the pH_{PZC} value, the surface becomes negative [32].

Figure 5(c) shows the effect of pH, in the range from 2 to 9, with a fixed weight of each photocatalyst (10 mg) and 10 mL solution volume of 100 mg/L MO at 25 °C under the influence of light. As shown in Fig. 6c, the degradation takes place over wide pH values (2-9). There is a minor difference in the degradation efficiency from acidic to basic medium for all the tested materials. The maximum degradation efficiency was achieved in acidic media at $pH \leq 4$, which is understandable considering the high concentration of H^+ adsorbed on the surface of the photocatalyst, making the surface positively charged. These positively charged surfaces facilitate the migration of light-generated e^-, which could interact with adsorbed O_2 to produce $^{\bullet}O_2^-$ ($e^- + O_2 \rightarrow {}^{\bullet}O_2^-$) [4]. Also, the positively charged surfaces could suppress the recombination of e^- and h^+, creating more $OH^{\bullet}$ through the reaction between h^+ and water. Both radical ions $^{\bullet}O_2^-$ and $OH^{\bullet}$ could be responsible for the increased MO degradation as strong oxidants. Moreover, the MO molecule exists in the quinoid form in acidic media at $pH \leq 4$ [33]. Similarly, in an alkaline medium, the negatively charged surfaces are suitable for the migration of the h^+ to TiO_2 surface and the production of $OH^{\bullet}$ [34]. This also facilitates MO degradation due to the

electrostatic attraction between the positively charged catalyst surfaces and MO anions [35]. When excited by light, TiO_2 generates e^- from the valence band (VB) to the conduction band (CB) and the retention of h^+ on the VB. Simultaneously, Co was easily photo-excited because light absorption was enhanced, particularly in the visible range, when photo-induced electrons were injected into the (CB) of TiO_2. The e^- could react with O_2 to produce $O_2^{\cdot-}$, while OH^- was created as a result of the action of H_2O. Furthermore, H_2O might capture h^+, resulting in $OH^{\cdot}$. As a result, h^+, $^{\bullet}O_2^-$, and OH^- might co-exist as active species and interact with the MO dye molecule, producing CO_2 as the reaction product. Similar findings have been reported in the literature [36]. The N-C bond in the dimethylamino [-N-$(CH_3)_2$] group breaks, and the methyl groups are replaced by protons [37]. Also, the photocatalytic reaction breaks the N=N bond and creates a number of intermediates. Reactive oxygen species might assault these intermediates, resulting in the formation of inorganic chemicals[38].

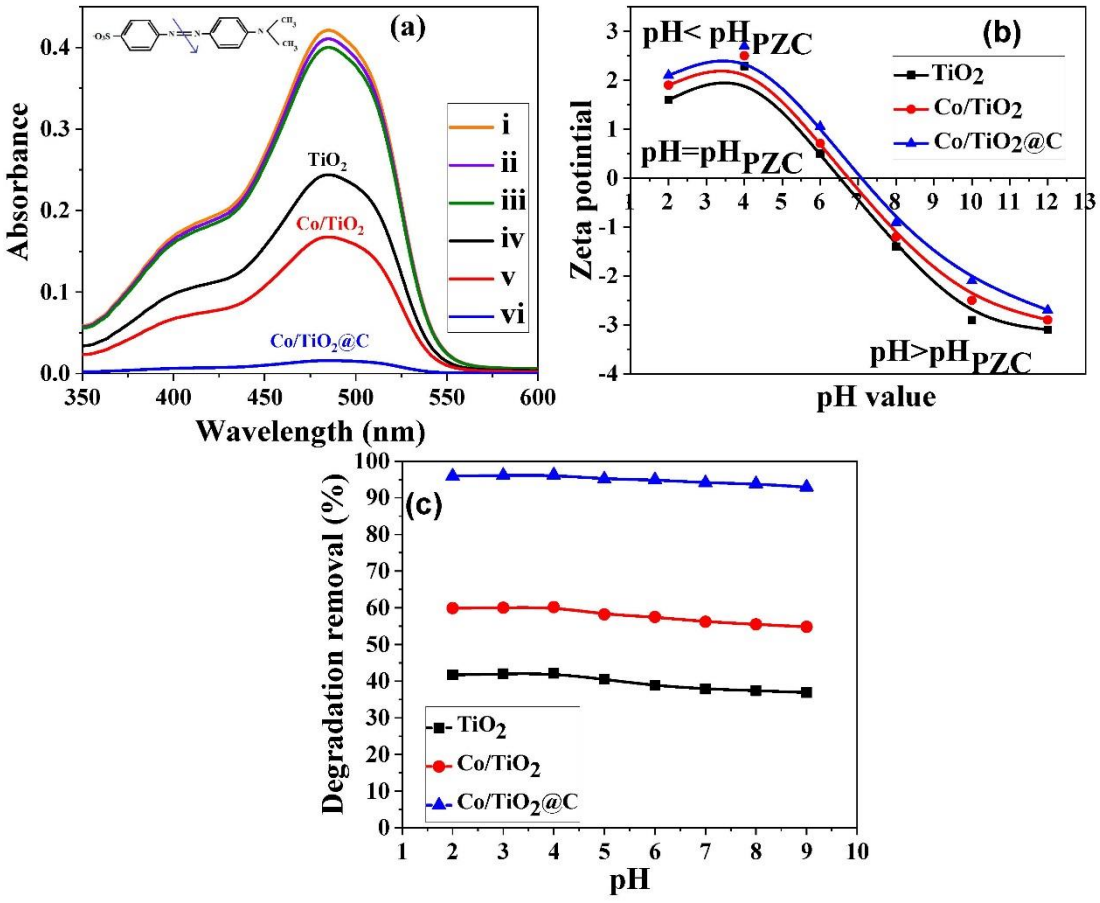

Fig. 5 (a) absorption spectra during the degradation process of MO dye: (i) MO dye (blank), (ii) MO after UV irradiation, (iii) MO degradation using TiO_2 in dark, (iv) MO degradation

using TiO_2 using UV irradiation, (v) MO degradation using Co/TiO_2 and (vi) MO using Co/TiO_2@C. (b) Zeta potential of TiO_2, Co/TiO_2, and Co/TiO_2@C catalysts in 0.01 M KCl as a function of pH. (c) The effect of pH on the degradation of MO using the synthesised TiO_2, Co/TiO_2, and Co/TiO_2@C photocatalysts at the optimal experimental condition.

The photocatalytic activities of various photocatalysts were studied against the contact time. As can be seen from (Fig. 6a), within the first 15 min, the amount of MO decreased by 10.1, 15.3, and 46.45% when TiO_2 and Co/TiO_2, and Co/TiO_2@C were used as photocatalysts, respectively. By increasing the contact time to 60 min, Co/TiO_2@C achieved the best efficiency of 96.2 % removal. The undoped TiO_2 and mono-doped Co/TiO_2 were 42.1 and 60.2%, respectively. To shade more light on the kinetic of the photodegradation process, the concentration ratio C/C_o, where C_o is the concentration measured at the start of light irradiation, is plotted against the contact time t in Fig. 6(b). The removal data of MO dye using TiO_2, Co/TiO_2, and Co/TiO_2@C is applied to the pseudo-first-order model, and the values of R^2 is calculated to be > 0.98, suggesting the photodegradation process was well-fitted with the pseudo-first-order kinetic model (eq. 1):

$$ln\,(C/Co\,) = -Kt \qquad (1)$$

where C_o is the initial concentration, C is the concentration after the exposure to light at time t, and K is the rate constant. From the linear relationship between $ln(C/C_o)$ and t, a straight line has been obtained with a slope that can be used to calculate the values of K (Fig. 6b). At pH 4 the Co/TiO_2@C has the highest apparent reaction rate constant of 5.45×10^{-2} min^{-1}, which is ~three times that of the mono-doped Co/TiO_2, further proving the enhancement of the degradation with the induced defects in the binary oxide (Table S1).

The effect of the initial MO concentrations on the photocatalytic behaviour of Co/TiO_2@C is a key factor in evaluating the MO degradation efficiency. The impact of the initial concentration on the MO removal using Co/TiO_2@C was studied at the optimal operating conditions (i.e., pH 4, contact time 60 min at 25°C). The results (Fig. 6c) indicate the MO removal efficiency and rate decrease with increasing the initial concentration, with the ability to remove almost all the

MO from the solution at concentrations less than or equal to 100 mg/l. These are not surprising results considering the fixed loading of the photocatalysts. The photocatalyst surfaces are probably crowded by the adsorbed substances and the reaction products, hindering the MO diffusion and slowing down further removal. Interestingly, the degradation efficiency is higher at any concentration when Co/TiO_2@C is the catalyst. This is because the enhanced conductivity of the composite by the induced oxygen vacancies effectively enhances the reaction kinetics on the catalyst surface, leading to a fast product removal. The maximum efficiency obtained for MO degradation in this study is found to be superior when compared to the relevant literature and studies, as shown in Table S2.

It is important to recover the catalysts and use them several times with reasonable efficiency for practical application. Co/TiO2@C photocatalyst's durability and reusability were studied after several repeating cycles. Between the cycles, the catalysts were recovered by light washing in dilute nitric acid solution. In Fig. 6(d), after 5 removal cycles, the efficiency of the Co/TiO_2@C photocatalyst reduced to only 96.2 % of the value of the fresh materials, indicating the reusability of the designed catalyst. The slight reduction in the performance after repeated cycles is believed to be due to the loss in adsorption sites as a result of the difficulties in eliminating degradation by-products from Co/TiO_2@C photocatalyst surfaces such as sulphur-containing materials. The experimental results demonstrated that the catalyst Co/TiO_2@C could be used in the MO degradation process with little efficiency loss and high durability.

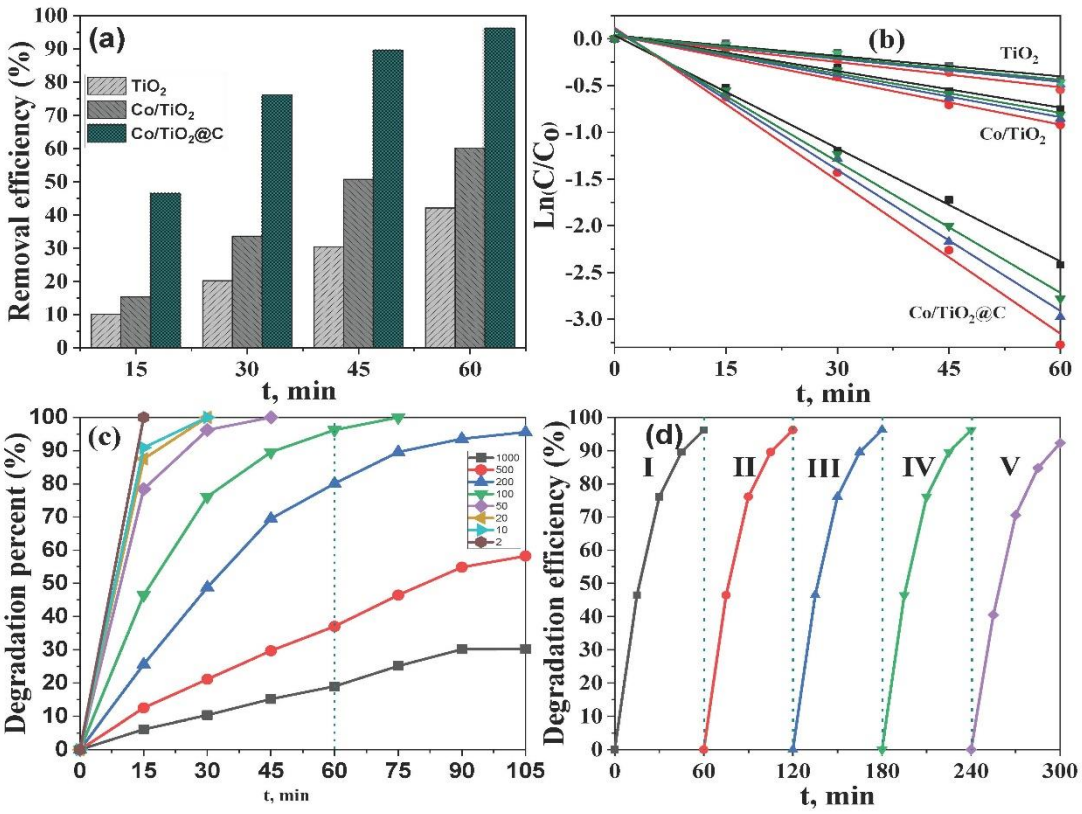

Fig. 6 (a) Removal efficiency of the synthesized photocatalysts, (b) pseudo-first-order of photo-degradation MO using TiO_2, Co/TiO_2 and Co/TiO_2@C photo-catalysts at different pH values. (c) Degradation efficiency (%) of Co/TiO_2@C photo-catalyst as a function of initial concentration at pH 4. (d) Reusability studies of Co/TiO_2@C photo-catalyst.

4- Conclusion

The Co-doped TiO_2 with induced oxygen vacancies photocatalysts was successfully synthesised via the simple hydrothermal method and used for the degradation of MO dye. The formation and crystallinity of synthesised catalytic composites were confirmed. Because of the large surface area and small band gab energy, as well as the facile electron transfer, Co/TiO_2@C demonstrated excellent catalytic performance with the ability to remove 96.2 %. In comparison, the Co-doped TiO_2 (without oxygen vacancies) and pure TiO_2 were able to remove only 60.2 % and 42.1 % of the dye, respectively. The catalytic degradation process was found to be compatible with the pseudo-first-order model, implying that MO might be degraded more readily. Furthermore, the produced catalyst demonstrated outstanding recycling capability for

up to five times usage. As a result, Co/TiO_2@C composites promise to remove organic contaminants from wastewater, benefiting both water remediation and waste management.

References

[1] M.G. Alalm, R. Djellabi, D. Meroni, C. Pirola, C.L. Bianchi, D.C. Boffito, Toward scaling-up photocatalytic process for multiphase environmental applications. Catalysts, 11 (2021) 562.

[2] T. Li, L. Zhao, Y. He, J. Cai, M. Luo, J. Lin, Synthesis of g-C_3N_4/$SmVO_4$ composite photocatalyst with improved visible light photocatalytic activities in RhB degradation. Applied Catalysis B: Environmental, 129 (2013) 255-263.

[3] Y. He, J. Cai, T. Li, Y. Wu, H. Lin, L. Zhao, M. Luo, Efficient degradation of RhB over $GdVO_4$/g-C_3N_4 composites under visible-light irradiation. Chemical engineering journal, 215 (2013) 721-730.

[4] Z. Feng, L. Zeng, Q. Zhang, S. Ge, X. Zhao, H. Lin, Y. He, In situ preparation of g-C_3N_4/$Bi_4O_5I_2$ complex and its elevated photoactivity in Methyl Orange degradation under visible light. Journal of Environmental Sciences, 87 (2020) 149-162.

[5] M. Sturini, A. Speltini, F. Maraschi, A. Profumo, L. Pretali, E.A. Irastorza, E. Fasani, A. Albini, Photolytic and photocatalytic degradation of fluoroquinolones in untreated river water under natural sunlight. Applied Catalysis B: Environmental, 119 (2012) 32-39.

[6] Z. Yu, F. Li, Q. Yang, H. Shi, Q. Chen, M. Xu, Nature-mimic method to fabricate polydopamine/graphitic carbon nitride for enhancing photocatalytic degradation performance. ACS Sustainable Chemistry & Engineering, 5 (2017) 7840-7850.

[7] F. Xu, Y. Yuan, H. Han, D. Wu, Z. Gao, K. Jiang, Synthesis of ZnO/CdS hierarchical heterostructure with enhanced photocatalytic efficiency under nature sunlight. CrystEngComm, 14 (2012) 3615-3622.

[8] C. Liu, Q. Zhang, W. Hou, Z. Zou, 2D Titanium/Niobium Metal Oxide-Based Materials for Photocatalytic Application. Solar RRL, 4 (2020) 2000070.

[9] H. Jing, Q. Cheng, J.M. Weller, X.S. Chu, Q.H. Wang, C.K. Chan, Synthesis of TiO_2 nanosheet photocatalysts from exfoliation of TiS_2 and hydrothermal treatment. Journal of Materials Research, 33 (2018) 3540-3548.

[10] R. Jain, M. Shrivastava, Photocatalytic removal of hazardous dye cyanosine from industrial waste using titanium dioxide. Journal of Hazardous materials, 152 (2008) 216-220.

[11] J. Zhang, P. Zhou, J. Liu, J. Yu, New understanding of the difference of photocatalytic activity among anatase, rutile and brookite TiO_2. Physical Chemistry Chemical Physics, 16 (2014) 20382-20386.

[12] H. Tada, M. Tanaka, Dependence of TiO_2 photocatalytic activity upon its film thickness. Langmuir, 13 (1997) 360-364.

[13] J. Leal, Y. Cantu, D. Gonzalez, J. Parsons, Brookite and anatase nanomaterial polymorphs of TiO_2 synthesized from $TiCl_3$. Inorganic Chemistry Communications, 84 (2017) 28-32.

[14] R. Raliya, C. Avery, S. Chakrabarti, P. Biswas, Photocatalytic degradation of methyl orange dye by pristine titanium dioxide, zinc oxide, and graphene oxide nanostructures and their composites under visible light irradiation. Applied Nanoscience, 7 (2017) 253-259.

[15] R. Asahi, T. Morikawa, T. Ohwaki, K. Aoki, Y. Taga, Visible-light photocatalysis in nitrogen-doped titanium oxides. science, 293 (2001) 269-271.

[16] X. An, C.Y. Jimmy, Graphene-based photocatalytic composites. Rsc Advances, 1 (2011) 1426-1434.

[17] G. Zhuang, J. Yan, Y. Wen, Z. Zhuang, Y. Yu, Two-Dimensional Transition Metal Oxides and Chalcogenides for Advanced Photocatalysis: Progress, Challenges, and Opportunities. Solar RRL, 5 (2021) 2000403.

[18] S.M. Adyani, and M. Ghorbani, A comparative study of physicochemical and photocatalytic properties of visible light responsive Fe, Gd P single and tri-doped TiO_2 nanomaterials. Journal of Rare Earths, 36 (2018) 72-85.

[19] R. Lontio Fomekong, B. Saruhan, Synthesis of Co^{3+} doped TiO_2 by co-precipitation route and its gas sensing properties. Frontiers in Materials, 6 (2019) 252.

[20] A. Hazra, K. Dutta, B. Bhowmik, V. Manjuladevi, R. Gupta, P. Chattopadhyay, P. Bhattacharyya, Structural and optical characterizations of electrochemically grown connected and free-standing TiO_2 nanotube array. Journal of electronic materials, 43 (2014) 3229-3235.

[21] P. Monazzam, B.F. Kisomi, Co/TiO_2 nanoparticles: preparation, characterization and its application for photocatalytic degradation of methylene blue. 63 (2017) 283-292.

[22] K. Sakurai, M. Mizusawa, X-ray diffraction imaging of anatase and rutile. Analytical chemistry, 82 (2010) 3519-3522.

[23] Q. Chen, L. Eisenach, M.J. Aziz, Cycling analysis of a quinone-bromide redox flow battery. Journal of The Electrochemical Society, 163 (2015) 5057-5063.

[24] Y. Yang, Q. Zhang, B. Zhang, W. Mi, L. Chen, L. Li, C. Zhao, E. Diallo, X. Zhang, The influence of metal interlayers on the structural and optical properties of nano-crystalline TiO_2 films. Applied Surface Science, 258 (2012) 4532-4537.

[25] M.S. Zoromba, M.H. Abdel-Aziz, M. Bassyouni, S. Gutub, D. Demko, A. Abdelkader, Electrochemical activation of graphene at low temperature: the synthesis of three-dimensional nanoarchitectures for high performance supercapacitors and capacitive deionization. ACS Sustainable Chemistry & Engineering, 5 (2017) 4573-4581.

[26] S.S. Chang, B. Clair, J. Ruelle, J. Beauchêne, F. Di Renzo, F. Quignard, G.-J. Zhao, H. Yamamoto, J. Gril, Mesoporosity as a new parameter for understanding tension stress generation in trees. Journal of experimental botany, 60 (2009) 3023-3030.

[27] M. Nasir, S. Bagwasi, Y. Jiao, F. Chen, B. Tian, J. Zhang, Characterization and activity of the Ce and N co-doped TiO_2 prepared through hydrothermal method. Chemical Engineering Journal, 236 (2014) 388-397.

[28] J. Qu, K. Zhang, H. Gamal, J. Wang, A.M. Abdelkader, Triple-shell NiO hollow sphere for p-type dye-sensitized solar cell with superior light harvesting. Solar Energy, 216 (2021) 238-244.

[29] L. Chen, X. Dai, X. Li, J. Wang, H. Chen, X. Hu, H. Lin, Y. He, Y. Wu, M. Fan, A novel Bi_2S_3/$KTa_{0.75}Nb_{0.25}O_3$ nanocomposite with high efficiency for photocatalytic and piezocatalytic N_2 fixation. Journal of Materials Chemistry A, 9 (2021) 13344-13354.

[30] L. Chen, W. Zhang, J. Wang, X. Li, Y. Li, X. Hu, L. Zhao, Y. Wu, Y. He, High piezo/photocatalytic efficiency of Ag/Bi_5O_7I nanocomposite using mechanical and solar energy for N_2 fixation and methyl orange degradation. Green Energy & Environment, 2021. doi: 10.1016/j.gee.2021.04.009.

[31] X. Dai, L. Chen, Z. Li, X. Li, J. Wang, X. Hu, L. Zhao, Y. Jia, S.-X. Sun, Y. Wu, $CuS/KTa_{0.75}Nb_{0.25}O_3$ nanocomposite utilizing solar and mechanical energy for catalytic N_2 fixation. Journal of Colloid and Interface Science, 603 (2021) 220-232.

[32] E.A. Elshehy, Hexagonal Cylinder Mesoporous Sorbent for Separation of Uranium Ions from Nitrate Media. Chemical Engineering & Technology, 44 (2021) 1470-1478.

[33] P. Salvador, On the nature of photogenerated radical species active in the oxidative degradation of dissolved pollutants with TiO_2 aqueous suspensions: a revision in the light of the electronic structure of adsorbed water. The Journal of Physical Chemistry C, 111 (2007) 17038-17043.

[34] N. Barka, A. Assabbane, A. Nounah, J. Dussaud, Y.A. Ichou, Photocatalytic degradation of methyl orange with immobilized TiO_2 nanoparticles: effect of pH and some inorganic anions. Phys. Chem. News, 41 (2008) 85-88.

[35] B. Wang, M. Xu, C. Chi, C. Wang, D. Meng, Degradation of methyl orange using dielectric barrier discharge water falling film reactor. Journal of Advanced Oxidation Technologies, 20(2) (2017).

[36] V. Vinesh, A. Shaheer, B. Neppolian, Reduced graphene oxide (rGO) supported electron deficient B-doped TiO_2 ($Au/B\text{-}TiO_2/rGO$) nanocomposite: an efficient visible light sonophotocatalyst for the degradation of Tetracycline (TC). Ultrasonics Sonochemistry, 50 (2019) 302-310.

[37] L.V. Trandafilović, D.J. Jovanović, X. Zhang, S. Ptasińska, M. Dramićanin, Enhanced photocatalytic degradation of methylene blue and methyl orange by ZnO: Eu nanoparticles. Applied Catalysis B: Environmental, 203 (2017) 740-752.

[38] K. Kaviyarasan, V. Vinoth, T. Sivasankar, A.M. Asiri, J.J. Wu, S. Anandan, Photocatalytic and photoelectrocatalytic performance of sonochemically synthesized $Cu_2O@TiO_2$ heterojunction nanocomposites. Ultrasonics Sonochemistry, 51 (2019) 223-229.